Surface States and Anisotropic Magnetoresistance in Nodal-Line Semimetal ZrGeTe

Ye Yang(杨野), and Hong Zhang(张红)*

College of Physics, Sichuan University, Chengdu 610065, China

Corresponding author: Hong Zhang, E-mail: hongzhang@scu.edu.cn

We investigate the electronic structure, anisotropic magnetoresistance (MR) and topological properties of nodal-line semimetal ZrGeTe using first-principles calculations. The band structure reveals a nodal line predominantly derived from the d orbitals of Zr and the p orbitals of Te and Ge. Surface state calculations confirm the topological signature through pronounced drumhead surface states, which exhibit a clear spin splitting after including spin-orbit coupling. The anisotropic MR is analyzed based on the calculated Fermi surface geometry. With current along the *c*-axis and magnetic field rotating in the *a*-*b* plane, the MR reflects the C_{4z} symmetry of the Fermi surface, reaching a maximum at $\varphi = 0$ and a minimum at $\varphi = \pi/4$. With current along the a or *b* axis and field rotating in the *a*-*c* plane, a butterfly-shaped MR pattern emerges, consistent with the twofold Fermi surface symmetry. Our results demonstrate that the complex Fermi surface geometry profoundly shapes the anisotropic MR of ZrGeTe.

Keywords：nodal-Line Semimetal, surface States, anisotropic magnetoresistance

PACS：71.15.Mb, 73.20.At, 72.15.Gd, 71.20.Ps

I.INTRODUCTION

Topological semimetals (TSMs) have attracted intense interest owing to their distinctive electronic structures and unconventional transport properties[1-6]. Unlike conventional metals or insulators, TSMs host topologically protected band crossings near the Fermi level, leading to

phenomena such as ultrahigh mobility[7, 8], giant magnetoresistance[7], and nonsaturating magnetoresistance[9]. Depending on the dimensionality of these crossings, TSMs are classified into Dirac semimetals[10-12], Weyl semimetals (chiral point nodes)[13-15], and nodal-line semimetals (one-dimensional line nodes)[16-23].

Among nodal-line semimetals, the one-dimensional band crossings form continuous closed loops in momentum space and are often protected by symmetries. This unique structure provides an ideal platform for studying low-energy excitations[24] and holds promise for applications in spintronics[25] and quantum computing[26].

Nodal-line semimetals have been predicted and experimentally confirmed in various material systems, including the ZrSiS family[27-32], $PbTaSe_2$[33-35], and Ca_3P_2[36, 37]. Among them, the ZrSiS family has emerged as a model system owing to its simple tetragonal structure and well-defined nodal rings protected by nonsymmorphic symmetries near the Fermi level, as extensively verified by angle-resolved photoemission spectroscopy (ARPES) and transport measurements.

Current research has primarily focused on ZrSiS and its isostructural counterparts, such as ZrSiSe and HfSiS[38-40]. In contrast, ZrGeTe has been only partially studied[41-43], and its magnetotransport properties remain unexplored. Although ZrGeTe also exhibits nodal-line semimetal features, systematic studies on its topological electronic structure, nodal-line configuration, and transport properties are still lacking. Moreover, the substitution of Te for S introduces stronger spin-orbit coupling (SOC), which may significantly affect the stability and topology of the nodal lines.

Against this background, we systematically investigate the topological electronic structure and physical properties of ZrGeTe, a nodal-line semimetal. Using first-principles calculations, we map

the band structure near the Fermi level, determine the spatial distribution and topological nature of the nodal lines, and examine the effect of spin-orbit coupling (SOC) on these features. We further study the magnetotransport properties of ZrGeTe to clarify their relation to the nodal-line electronic structure.

Our results show that, without SOC, ZrGeTe is a typical nodal-line semimetal with nodal lines located in high-symmetry planes of the Brillouin zone. A well-defined drumhead surface state, which has not been reported previously, is obtained from our calculations. When SOC is included, the nodal lines are almost fully gapped, leaving only two Dirac points along the Γ–Z direction that are protected by symmetry. This indicates that ZrGeTe transforms from a nodal-line semimetal into a Dirac semimetal under SOC. The calculated Fermi surface geometry further suggests the existence of anisotropic magnetoresistance (AMR) in ZrGeTe. These findings not only deepen the understanding of topological semimetals in the ZrSiS family, but also provide theoretical insights into the effects of heavy-element substitution on nodal-line states, potentially advancing the exploration of nodal-line semimetals for low-power electronic applications.

II. METHOD

To investigate the electronic structure and topological properties, first-principles calculations were performed using density functional theory (DFT) as implemented in the Vienna Ab initio Simulation Package (VASP)[44]. The exchange-correlation functional was treated using the generalized gradient approximation (GGA) in the form of the Perdew–Burke–Ernzerhof (PBE) functional[45]. The projector augmented wave (PAW) method was employed to describe the electron–ion interactions[46]. A plane-wave cutoff energy of 600 eV was used, and the Brillouin zone was sampled with a Γ-centered k-mesh of 25 × 25 × 11. The total energy convergence criterion was set

to 10^{-9} eV. The maximally localized Wannier functions were constructed using the Wannier90 code[47-49]. The nodal line distribution, surface states, and anisotropic magnetoresistance were calculated using the Wannier Tools package[50]. In addition, the Irvsp code was used to obtain the irreducible representations of the band structure for symmetry analysis[51].

III. RESULTS AND DISCUSSIONS

A. CRYSTAL AND BAND STRUCTURE OF ZrGeTe

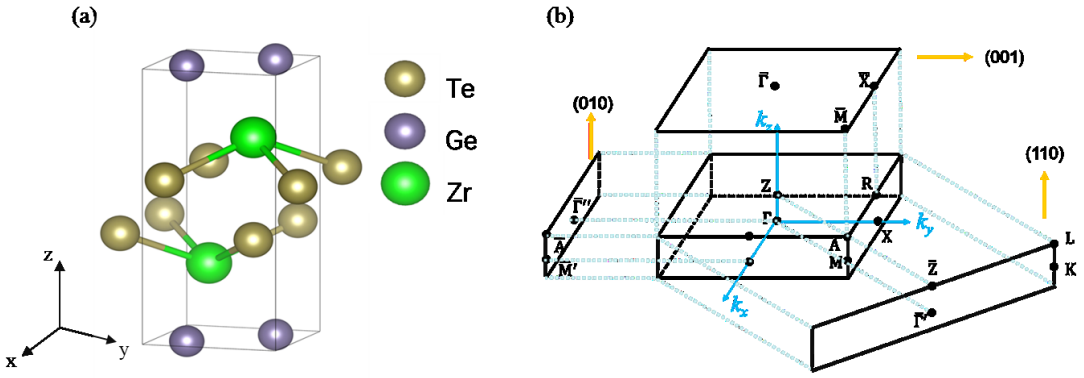


FIG. 1. (a) The primitive cell of ZrGeTe. (b) Brillouin zone of ZrGeTe and projections of (001), (010), and (110) surfaces.

There are 2 Zr, 2 Ge and 2 Te atoms in the primitive cell of ZrGeTe as illustrated in Fig. 1(a). Its space group is tetragonal *P*4/*nmm*(No.129) which is comprised of inversion symmetry, four mirror reflections, glide mirror reflection, three twofold screw rotations, two twofold rotations, fourfold rotation and two fourfold rotoinversions. The optimized lattice constants are $a = b =$ 3.866020 Å and c = 8.599050 Å, agreeing well with experimental data ($a = b$ = 3.866Å and c = 8.599Å)[41]. The Brillouin zone (BZ) of ZrGeTe and its projections are exhibited in Fig. 1(b). We first performed first-principles calculations of the electronic band structure of ZrGeTe. Figs. 2(a) show the bulk band structures without SOC. The band gap between the 22nd and 23rd bands is

filled with colored shading because a unit cell contains 22 valence electrons. From the band structure shown in Fig. 2(a), it can be observed that there are six nodes located at Γ-X, M-Γ, M-Γ, Γ-Z, Z-R and A-Z, respectively. Due to the existence of *PT* symmetry in this system, these six Dirac points strongly suggest the possible existence of the nodal line near the Fermi level.

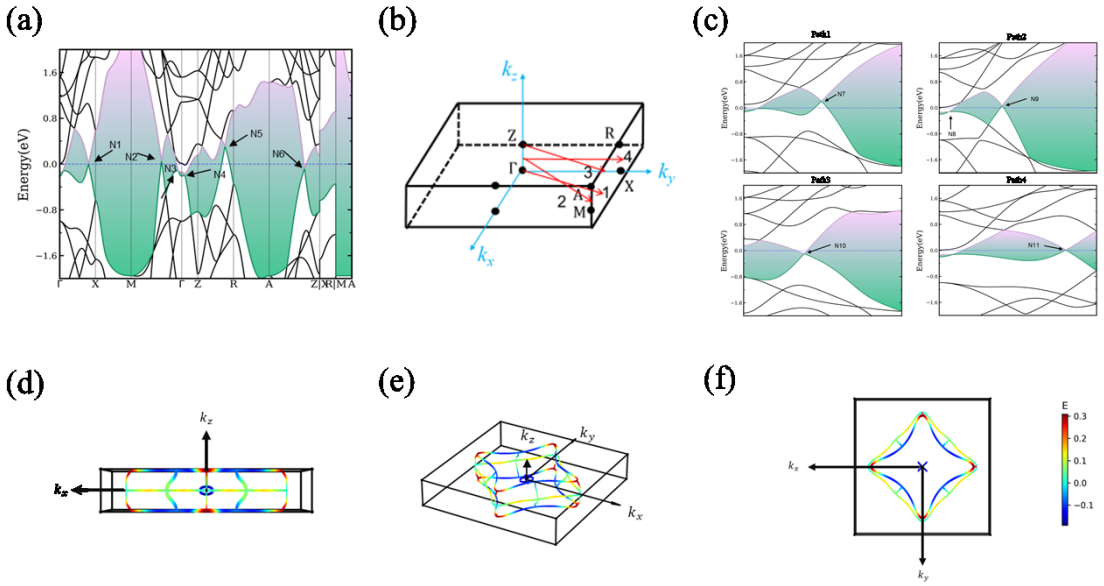


FIG. 2. (a) Band structure of ZrGeTe calculated without SOC. The gap between N_{occ} and N_{occ+1} bands is filled with green shading. Black arrows mark the band crossings. (b) Schematic of the bulk Brillouin zone showing four paths (red lines), which are defined as: Path1 from (0, 0, 0) to (0.3, 0.5, 0); Path2 from (0, 0, 0.03) to (0.5, 0.5, 0.03); Path3 from (0, 0, 0.5) to (0.3, 0.5, 0.5); Path4 from (0, 0, 0.03) to (0, 0.5, 0.03). (c) Calculated band dispersions along the four generic paths Path1 to Path4. The black arrows mark the band crossings. (d) Side view of the nodal line in the Brillouin zone. (e) Perspective view of the nodal line. (f) Top view of the nodal line. Colors represent the energy relative to the Fermi level (E_F). (Red: above E_F; blue: below E_F.).

To further confirm this, a nodal-line search was performed in the whole Brillouin zone by identifying all k-points with an energy gap below the threshold of 0.0001 eV between these two

bands. The nodal-line structure is shown in Figs. 2(d), 2(e) and 2(f), from which it can be observed that several nodal lines form a complex nodal-net. In the $k_z = 0$ plane, there exists a single nodal line with an approximately diamond-shaped geometry. In the $k_z = \pi / c$ plane, a nodal line forms a concave, diamond-like loop. In each of these two planes $\{m_{1\bar{1}0}\}$ and $\{m_{110}\}$, two small nodal loops are present. These loops touch each other at two crossing points lying on the k_z -axis. Moreover, two pairs of nodal lines extend along the k_z direction, connecting the diamond-like loop at $k_z = 0$ and the concave diamond-like loop at $k_z = \pi / c$. In addition, similar connecting nodal lines are also present in the $k_x = 0$ and $k_y = 0$ planes, forming a three-dimensional cage-like nodal-line network in the bulk Brillouin zone. In contrast to ZrSiS[52], the nodal-line structure of ZrGeTe contains two extra small nodal rings encircling the Γ point. To investigate the formation mechanism of these band crossing points, orbital-character analysis was performed. As shown in the Figs. 3, N1 is dominated by Zr-d_{xz}, Ge-p_x, Ge-p_y, and Te-p_z orbitals; N2 is dominated by Zr-d_{x2-y2}, Zr-d_{yz} and Ge-p_y orbitals; N3 and N4 are dominated by Zr-d_{x2-y2}, Ge-s, Ge-p_z, and Te-p_z orbitals; N5 is dominated by Zr-d_{xz}, Zr-d_{x2-y2}, Ge-p_x, Ge-p_y and Te-p_z orbitals; N6 is dominated by Zr-d_{z2}, Zr-d_{x2-y2}, Ge-p_y, and Te-p_y orbitals, respectively. The foregoing analysis demonstrates that the nodal line is predominantly derived from the d orbitals of Zr and the p orbitals of Te and Ge.

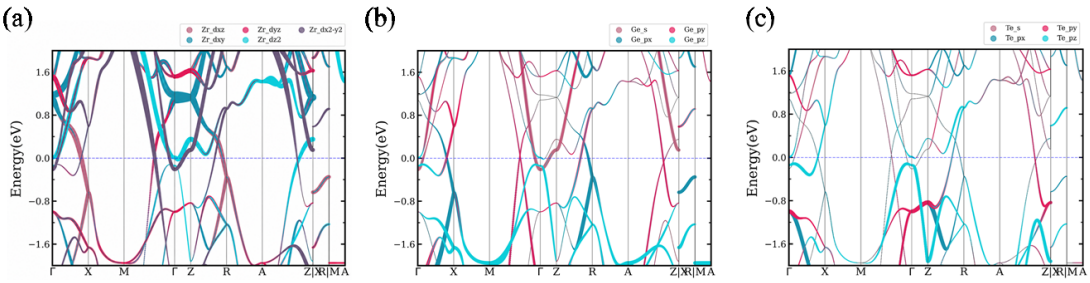


FIG. 3. Fatband analysis of ZrGeTe with the spectral weight projected onto: (a) Zr, (b) Ge, and (c) Te.

B. Topological Properties and Surface States

Next, we examine whether the nodal line is topologically trivial. Therefore, a loop encircling for every nodal line is selected to compute the Berry phase. The Berry phase accumulated along the encircling path is π[18, 19], which confirms the nontrivial topological nature of the nodal line. In addition, the theory of band representations (BR)[53], which is the basis of topological quantum chemistry (TQC)[54-57], provides a more general symmetry-based method to determine whether the system is topologically trivial or nontrivial. we further verified the topological feature of the nodal line by analyzing the irreducible representations of the energy bands. Both the N1 and N2 points belong to the nodal line located on the $k_z = 0$ plane, which are protected by the glide mirror symmetry $\{m_{001}|1/2, 1/2, 0\}$. To further validate the symmetry protection mechanism of the nodal lines, we analyzed the band crossings along a more generic path (Path1) in momentum space. We find that node N7 is similarly protected by the glide mirror symmetry. Since nodes N3, N4, and N8 all belong to the same nodal ring residing on this mirror plane $\{m_{1\bar{1}0}|0, 0, 0\}$, they share the same mirror symmetry protection. Consequently, the entire nodal ring is protected by the mirror symmetry. Likewise, the nodal line containing both N2 and N9 is also protected by the mirror symmetry $\{m_{1\bar{1}0}|0, 0, 0\}$. Nodes N5, N6, and N10 belong to the same nodal loop lying in the $k_z = \pi / c$ plane and are protected by the glide mirror symmetry $\{m_{001}|1/2, 1/2, 0\}$. Finally, nodes N1 and N11 are located on the nodal line within the $k_x = 0$ plane, whose degeneracy is protected by the mirror symmetry $\{m_{100}|1/2, 0, 0\}$. This comprehensive classification demonstrates that the observed band degeneracies are not accidental but are strictly enforced by the of space-group symmetries.

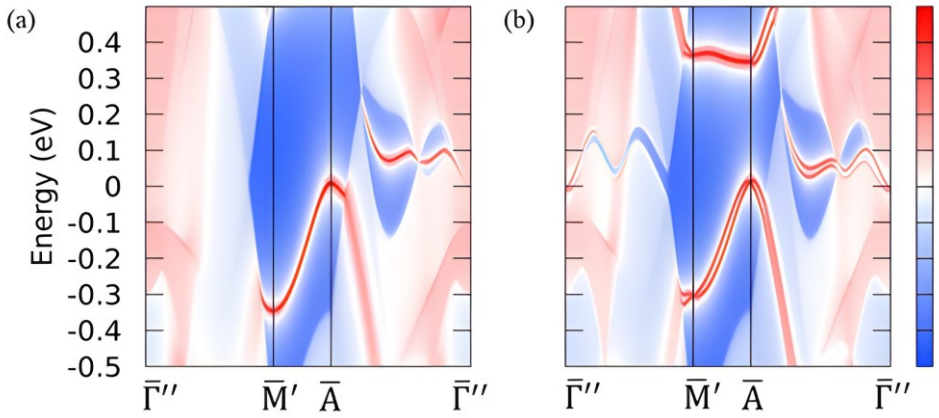


FIG. 4. (a) Surface spectrum of the (010) surface without SOC. Red indicates higher surface state density. (b) Surface spectrum of the (010) surface with SOC.

To identify the topological signature of the nodal line, we calculated the (010) surface states of ZrGeTe with and without SOC, as shown in Figs. 4(a) and 4(b). The nontrivial topology of the nodal line implies the existence of drumhead surface states within the projected nodal ring. The (010) surface was selected for the surface state calculations for two reasons. First, the nodal lines project onto the (010) surface Brillouin zone without overlapping, allowing the drumhead surface states to be clearly identified. Second, as noted in previous studies, the (001) surface states are difficult to reproduce in slab calculations because the small bulk SOC gap leads to a long penetration depth, and the resulting hybridization between the top and bottom surface states in a finite slab can strongly modulate the surface state dispersion[58]. The (010) surface does not suffer from this complication and is therefore better suited for identifying the intrinsic topological surface states. The surface states were calculated for different terminations of the (010) surface. Since the resulting drumhead surface states are essentially identical for all the terminations considered, only one termination is presented in the following discussion. As shown in Fig. 4(a), prominent drumhead surface states are observed inside the projection of the nodal ring. After the inclusion of SOC, the surface states display a clear spin splitting in the Fig. 4(b).

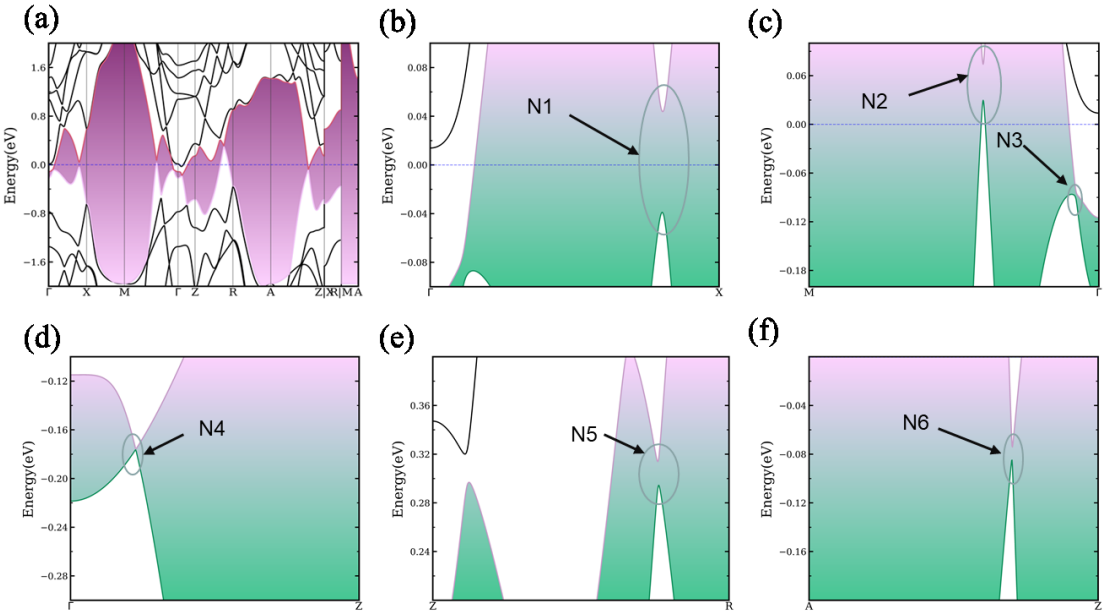


FIG. 5. (a) Band structure of ZrGeTe with spin–orbit coupling (SOC). Magnified views of the band structures including SOC along high-symmetry directions. (b) Γ-X. (c) M-Γ. (d) Γ-Z. (e) Z-R. (f) A-Z. The positions of the nodal points in the absence of SOC are highlighted with ellipses, showing where the band degeneracies are lifted by SOC.

We further performed a nodal-line search with SOC included using an energy threshold of 0.0001 eV. The search shows that only two nodal points remain, both located on the C_4 rotation axis. These surviving degeneracies are protected by the C_4 rotational symmetry, since the crossing bands have opposite C_4 eigenvalues and cannot be hybridized by SOC. The SOC band structure presented in Figs. 5 further confirms this result: among all the original nodal points, only N4 remains gapless, whereas all the other crossings are gapped out by SOC. This indicates that ZrGeTe transforms from a nodal-line semimetal into a Dirac semimetal under SOC. To quantitatively compare the SOC effect among the ZrSiS-family compounds, we selected the nodal point N1 located along the Γ–X direction as a representative crossing. The SOC-induced gaps at N1 are calculated to be 20 meV for ZrSiS[27], 50 meV for ZrSiSe [59], and 80 meV for ZrGeTe, respectively. Clearly, ZrGeTe exhibits the strongest SOC among the three compounds.

C. Anisotropic Magnetoresistance

Magnetoresistance in ZrSiX (X= S, Se, Te) nodal-line semimetals has been reported previously[60], the anisotropic MR of ZrGeTe remains unexplored. The nodal-line structure of ZrGeTe gives rise to a diamond-shaped Fermi surface. Fig. 6(a) shows the Fermi surface, and Figs. 6(b)–6(d) display its projections onto different planes. The structure of the Fermi surface strongly indicates that it is likely responsible for the observed anisotropic MR[61]. We therefore calculated the anisotropic MR, and the results are presented in Figs. 7.

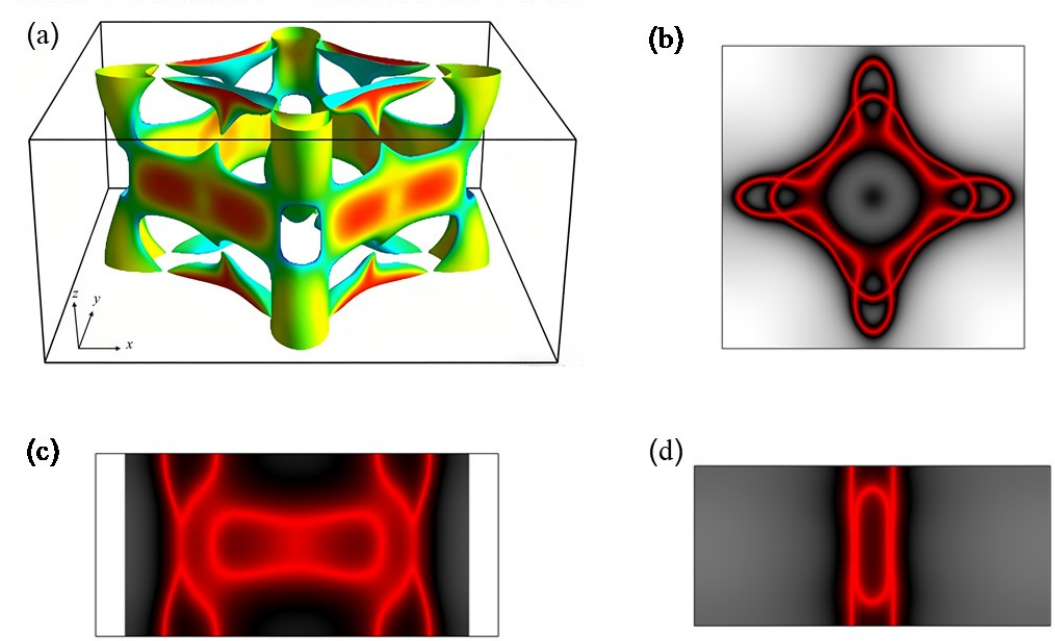


FIG. 6. (a) Fermi surface of ZrGeTe. (b) the projection of the (001) Fermi surface through (0, 0, 0.5). (c) the projection of the (110) Fermi surface through (0.4π/a, 0.4π/a, 0). (d) the projection of the (100) Fermi surface through (0.73π/a, 0, 0).

In the semiclassical framework, the electron velocity is proportional to the gradient of the band dispersion in k-space, written as

$$\boldsymbol{v}_n(\boldsymbol{k}) = \frac{1}{\hbar}\nabla_{\boldsymbol{k}}\varepsilon_n(\boldsymbol{k}), \tag{1}$$

Where $\boldsymbol{k}$ is the wave vector in the Brillouin zone, n is the band index. The conductivity tensor $\boldsymbol{\sigma}$ is computed from the Boltzmann equation under the relaxation-time approximation, with an external magnetic field included in the transport calculation

$$\boldsymbol{\sigma}^{(n)}(\boldsymbol{B}) = \frac{e^2}{4\pi^3}\int d\boldsymbol{k}\,\tau_n \boldsymbol{v}_n(\boldsymbol{k})\bar{\boldsymbol{v}}_n(\boldsymbol{k})\left(-\frac{\partial f}{\partial \varepsilon}\right)_{\varepsilon=\varepsilon_n(\boldsymbol{k})}. \tag{2}$$

Here e is the electron charge, τ_n is the relaxation time, f is the Fermi–Dirac distribution function, and $\bar{\boldsymbol{v}}_n(\boldsymbol{k})$ is the weighted average of velocity over the past history of the charge carrier

$$\bar{\boldsymbol{v}}_n(\boldsymbol{k}) = \int_{-\infty}^{0} \frac{dt}{\tau_n} e^{\frac{t}{\tau_n}} \boldsymbol{v}_n(\boldsymbol{k}(t)). \tag{3}$$

The orbital motion of charge carriers in applied magnetic field causes the time evolution of $\boldsymbol{k}_n(t)$, written as

$$\frac{d\boldsymbol{k}_n(t)}{dt} = -\frac{e}{\hbar} \boldsymbol{v}_n(\boldsymbol{k}(t)) \times \boldsymbol{B}. \tag{4}$$

In the semiclassical picture, the Lorentz force is perpendicular to the electron velocity $\boldsymbol{v}_n(\boldsymbol{k})$, and therefore the energy $\varepsilon_n(\boldsymbol{k})$ remains constant as the wave vector $\boldsymbol{k}$ evolves in time. From Eq. (1), the velocity $\boldsymbol{v}_n(\boldsymbol{k})$ is perpendicular to the constant-energy surface, and the time derivative of

$\boldsymbol{k}$ is perpendicular to the magnetic field. Consequently, the *k*-space trajectory of an electron is given by the Fermi surface cross-section perpendicular to $\boldsymbol{B}$. Thus, by analyzing the Fermi surface geometry in momentum space, we can gain insight into the charge transport in real space. First, we analyzed the anisotropic MR in Fig. 7(a), with current along the *c*-axis and magnetic field rotating in the *a*-*b* plane. The anisotropic MR is observed to be consistent with the C_{4z} symmetry of the Fermi surface in the *a*-*b* plane. The MR reaches its maximum when the magnetic field is aligned with the *a*-axis (φ = 0) and then decreases with increasing φ, reaching a minimum

at $\varphi = \pi/4$. As can be seen from Figs. 5(c) and 5(d), When the magnetic field is along the *a*-axis, the orbit in momentum space lies in the *b*–*c* plane. The Fermi surface cross-section in this plane contains open orbits extending along *c*-axis. Since the real-space velocity is perpendicular to the momentum-space orbit, these open orbits lead to the motion of charge carriers predominantly along the *b*-axis in real space. Consequently, the effective conduction along *c*-axis is strongly suppressed, giving rise to the large magnetoresistance in this configuration. At $\varphi = \pi/4$, a large number of *k*-space orbits on the Fermi surface cross-section have their normal directions tilted toward *c*-axis. This increases the effective conduction along *c*-axis and gives rise to the MR minimum.

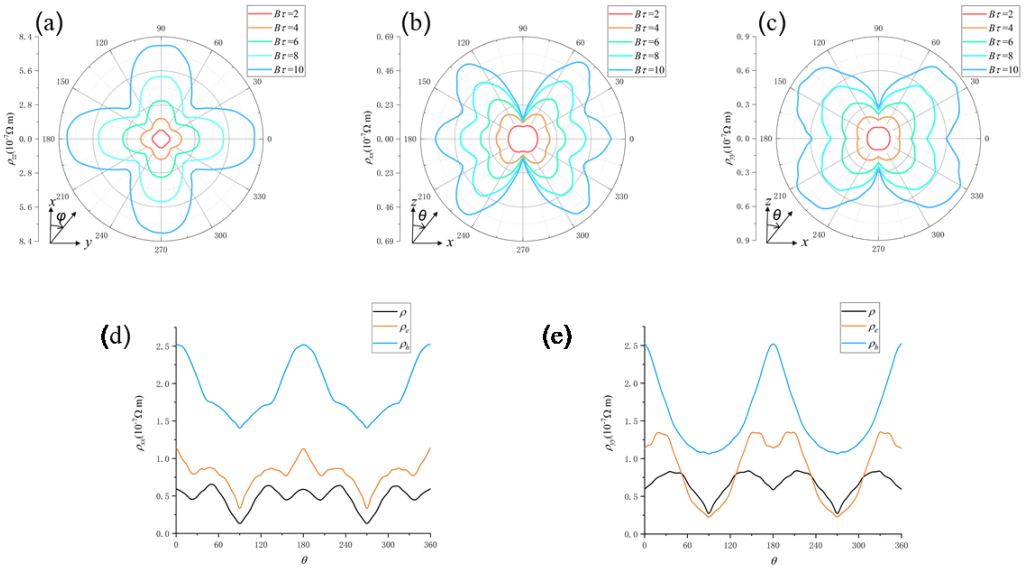


FIG. 7. Calculated anisotropic magnetoresistance of ZrGeTe for currents along (a) the *c*, (b) *a*, and (c) *b* axes, and magnetic field rotating in the *a*-*b*, *a*-*c*, and *a*-*c* planes, respectively. (d) Resistivity ρ_{xx} as a function of magnetic field orientation. (e) Resistivity ρ_{yy} as a function of magnetic field orientation.

Fig. 7(b) shows the polar plot of the anisotropic MR with the current applied along the *a*-axis and the magnetic field rotated within the *a*-*c* plane, exhibiting a butterfly-shaped MR pattern. In

contrast to ZrSiS[60], ZrGeTe shows a more pronounced MR maximum at $\theta = 0$ and reaches its maximum around at $\theta = \pi/4$, then decreases to its minimum at $\theta = \pi/2$. In particular, ZrGeTe exhibits a richer angular dependence with six prominent peaks in the a–c plane. Fig. 7(c) shows the polar plot of the anisotropic MR for current along the *b*-axis and magnetic field rotating in the *a*-*c* plane. The butterfly-shaped MR pattern is also observed, with the maximum again around $\theta = \pi/4$, the smaller minimum at $\theta = \pi/2$, and the larger minimum at $\theta = 0$. Because of the twofold symmetry of the Fermi surface in the *a*-*c* plane, the anisotropic MR also exhibits twofold symmetry when the magnetic field rotates within this plane. We also calculated the electron and hole contributions to the resistivity, as well as the total resistivity, as shown in Figs. 7(d) and 7(e). As can be seen from Figs. 7(d) and 7(e), the electron resistivity is much smaller than the hole resistivity, indicating that the electronic channel dominates the total resistivity. Based on our calculations, it can be seen that the complex Fermi surface geometry arising from the nodal line in ZrGeTe significantly influences its anisotropic MR.

IV. Conclusions

We systematically investigated the electronic structure, topological properties, and anisotropic magnetoresistance (MR) of the nodal-line semimetal ZrGeTe using first-principles calculations. The nodal line is formed by bands 22 and 23, predominantly derived from the d orbitals of Zr and the p orbitals of Te and Ge. Pronounced drumhead surface states on the (010) surface confirm the nontrivial topology, and these states exhibit a clear spin splitting after including spin-orbit coupling. The calculated Fermi surface geometry suggests an intrinsic origin for the anisotropic MR. With current along the *c*-axis and field rotating in the *a*–*b* plane, the MR reflects the C_{4z} symmetry of the Fermi surface, with the maximum at $\varphi = 0$ attributed to open orbits along

the *c*-axis. With current along the *a*- or *b*-axis and field rotating in the *a*–*c* plane, a butterfly-shaped MR pattern emerges, consistent with the twofold symmetry of the Fermi surface. Our results demonstrate that the intricate Fermi surface topology profoundly governs the anisotropic MR in ZrGeTe.

ACKNOWLEDGMENTS

We thank the support from the National Key Research and Development Program of China (2024YFF0508503) and Beijing National Laboratory for Condensed Matter Physics (Grant No. 2025BNLCMPKF025).

References

[1] Chiu C-K, Teo J C Y, Schnyder A P and Ryu S 2016 *Reviews of Modern Physics* **88** 035005
[2] Bansil A, Lin H and Das T 2016 *Reviews of Modern Physics* **88** 021004
[3] Armitage N P, Mele E J and Vishwanath A 2018 *Reviews of Modern Physics* **90** 015001
[4] Jiang W, Huang H, Liu F, Wang J-P and Low T 2020 *Physical Review B* **101** 121113
[5] Jiang W, de Sousa D J P, Wang J-P and Low T 2021 *Physical Review Letters* **126** 106601
[6] Zhu Y, Zhao B, Xue Y, Xu W, Xu W and Yang Z 2024 *Chinese Physics Letters* **41** 067301
[7] Liang T, Gibson Q, Ali M N, Liu M, Cava R J and Ong N P 2015 *Nature Materials* **14** 280
[8] Shekhar C, Nayak A K, Sun Y, Schmidt M, Nicklas M, Leermakers I, Zeitler U, Skourski Y, Wosnitza J, Liu Z, Chen Y, Schnelle W, Borrmann H, Grin Y, Felser C and Yan B 2015 *Nature Physics* **11** 645
[9] Ali M N, Xiong J, Flynn S, Tao J, Gibson Q D, Schoop L M, Liang T, Haldolaarachchige N, Hirschberger M, Ong N P and Cava R J 2014 *Nature* **514** 205
[10] Young S M and Kane C L 2015 *Physical Review Letters* **115** 126803
[11] Wieder B J, Kim Y, Rappe A M and Kane C L 2016 *Physical Review Letters* **116** 186402
[12] Wieder B J, Wang Z, Cano J, Dai X, Schoop L M, Bradlyn B and Bernevig B A 2020 *Nature Communications* **11** 627
[13] Xu S-Y, Belopolski I, Alidoust N, Neupane M, Bian G, Zhang C, Sankar R, Chang G, Yuan Z, Lee C-C, Huang S-M, Zheng H, Ma J, Sanchez D S, Wang B, Bansil A, Chou F, Shibayev P P, Lin H, Jia S and Hasan M Z 2015 *Science* **349** 613
[14] Weng H, Fang C, Fang Z, Bernevig B A and Dai X 2015 *Physical Review X* **5** 011029
[15] Li P, Wen Y, He X, Zhang Q, Xia C, Yu Z-M, Yang S A, Zhu Z, Alshareef H N and Zhang X-X 2017 *Nature Communications* **8** 2150
[16] Chiu C-K and Schnyder A P 2014 *Physical Review B* **90** 205136

[17] Takahashi R, Hirayama M and Murakami S 2017 *Physical Review B* **96** 155206
[18] Fang C, Weng H, Dai X and Fang Z 2016 *Chinese Physics B* **25** 117106
[19] Fang C, Chen Y, Kee H-Y and Fu L 2015 *Physical Review B* **92** 081201
[20] Burkov A A, Hook M D and Balents L 2011 *Physical Review B* **84** 235126
[21] Yu R, Weng H, Fang Z, Dai X and Hu X 2015 *Physical Review Letters* **115** 036807
[22] Gao X-J, Ge Y and Gao Y 2026 *Chinese Physics B* **35** 057110
[23] Hou X-Y, Gao Z-F, Guo P-J, Zhang J-F and Lu Z-Y 2026 *Chinese Physics B* **35** 017301
[24] Rahimpoor H and Abedinpour S H 2024 *Physical Review B* **109** 045120
[25] Chen J, Zhang R-W, Yu Z-M, Jiang W and Yao Y 2024 *Physical Review Materials* **8** 044201
[26] Maciejko J, Hughes T L and Zhang S-C 2011 *Annual Review of Condensed Matter Physics* **2** 31
[27] Schoop L M, Ali M N, Straßer C, Topp A, Varykhalov A, Marchenko D, Duppel V, Parkin S S P, Lotsch B V and Ast C R 2016 *Nature Communications* **7** 11696
[28] Neupane M, Belopolski I, Hosen M M, Sanchez D S, Sankar R, Szlawska M, Xu S-Y, Dimitri K, Dhakal N, Maldonado P, Oppeneer P M, Kaczorowski D, Chou F, Hasan M Z and Durakiewicz T 2016 *Physical Review B* **93** 201104
[29] Lou R, Ma J Z, Xu Q N, Fu B B, Kong L Y, Shi Y G, Richard P, Weng H M, Fang Z, Sun S S, Wang Q, Lei H C, Qian T, Ding H and Wang S C 2016 *Physical Review B* **93** 241104
[30] Topp A, Lippmann J M, Varykhalov A, Duppel V, Lotsch B V, Ast C R and Schoop L M 2016 *New Journal of Physics* **18** 125014
[31] Hosen M M, Dimitri K, Belopolski I, Maldonado P, Sankar R, Dhakal N, Dhakal G, Cole T, Oppeneer P M, Kaczorowski D, Chou F, Hasan M Z, Durakiewicz T and Neupane M 2017 *Physical Review B* **95** 161101
[32] Fu B-B, Yi C-J, Zhang T-T, Caputo M, Ma J-Z, Gao X, Lv B Q, Kong L-Y, Huang Y-B, Richard P, Shi M, Strocov V N, Fang C, Weng H-M, Shi Y-G, Qian T and Ding H 2019 *Science Advances* **5** eaau6459
[33] Bian G, Chang T-R, Sankar R, Xu S-Y, Zheng H, Neupert T, Chiu C-K, Huang S-M, Chang G, Belopolski I, Sanchez D S, Neupane M, Alidoust N, Liu C, Wang B, Lee C-C, Jeng H-T, Zhang C, Yuan Z, Jia S, Bansil A, Chou F, Lin H and Hasan M Z 2016 *Nature Communications* **7** 10556
[34] Zhang C-L, Yuan Z, Bian G, Xu S-Y, Zhang X, Hasan M Z and Jia S 2016 *Physical Review B* **93** 054520
[35] Wang H, Liu H, Feng X, Cao J, Wu W, Lai S, Gao W, Xiao C and Yang S A 2025 *Physical Review Letters* **134** 056301
[36] Chan Y H, Chiu C-K, Chou M Y and Schnyder A P 2016 *Physical Review B* **93** 205132
[37] Alassaf A, Koltai J, García-Fuente A and Oroszlány L 2024 *Scientific Reports* **14** 31845
[38] Linnartz J F, Kool A, Lorenz J P, Müller C S A, van Delft M R, Singha R, Schoop L M, Hussey N E, de Visser A and Wiedmann S 2024 *npj Quantum Materials* **9** 63
[39] Zhao M, Zhuang Z-Y, Wu F, Leng P, Joseph N B, Xie X, Ozerov M, He S, Chen Y, Narayan A, Liu Z and Xiu F 2024 *ACS Nano* **18** 16684
[40] Yang Y, Zhu P, Yang L, Liu J, Li Y and Wang Z 2022 *Crystals* **12** 728
[41] Yen Y, Chiu C-L, Lin P-H, Sankar R, Chuang T-M and Guo G-Y 2021 *New Journal of Physics* **23** 103019
[42] Hosen M M, Dimitri K, Aperis A, Maldonado P, Belopolski I, Dhakal G, Kabir F, Sims C,

Hasan M Z, Kaczorowski D, Durakiewicz T, Oppeneer P M and Neupane M 2018 *Physical Review B* **97** 121103

[43] Yang Z-M and Li H 2025 *Physica B: Condensed Matter* **718** 417914

[44] Kresse G and Furthmüller J 1996 *Physical Review B* **54** 11169

[45] Perdew J P, Burke K and Ernzerhof M 1996 *Physical Review Letters* **77** 3865

[46] Blöchl P E 1994 *Physical Review B* **50** 17953

[47] Marzari N and Vanderbilt D 1997 *Physical Review B* **56** 12847

[48] Souza I, Marzari N and Vanderbilt D 2001 *Physical Review B* **65** 035109

[49] Pizzi G, Vitale V, Arita R, Blügel S, Freimuth F, Géranton G, Gibertini M, Gresch D, Johnson C, Koretsune T, Ibañez-Azpiroz J, Lee H, Lihm J-M, Marchand D, Marrazzo A, Mokrousov Y, Mustafa J I, Nohara Y, Nomura Y, Paulatto L, Poncé S, Ponweiser T, Qiao J, Thöle F, Tsirkin S S, Wierzbowska M, Marzari N, Vanderbilt D, Souza I, Mostofi A A and Yates J R 2020 *Journal of Physics: Condensed Matter* **32** 165902

[50] Wu Q, Zhang S, Song H-F, Troyer M and Soluyanov A A 2018 *Computer Physics Communications* **224** 405

[51] Gao J, Wu Q, Persson C and Wang Z 2021 *Computer Physics Communications* **261** 107760

[52] Shao Y, Moon S, Rudenko A N, Wang J, Herzog-Arbeitman J, Ozerov M, Graf D, Sun Z, Queiroz R, Lee S H, Zhu Y, Mao Z, Katsnelson M I, Bernevig B A, Smirnov D, Millis A J and Basov D N 2024 *Physical Review X* **14** 041057

[53] Zhu Z, Cheng Y and Schwingenschlögl U 2012 *Physical Review B* **85** 235401

[54] Cano J, Bradlyn B, Wang Z, Elcoro L, Vergniory M G, Felser C, Aroyo M I and Bernevig B A 2018 *Physical Review B* **97** 035139

[55] Vergniory M G, Elcoro L, Wang Z, Cano J, Felser C, Aroyo M I, Bernevig B A and Bradlyn B 2017 *Physical Review E* **96** 023310

[56] Bradlyn B, Elcoro L, Cano J, Vergniory M G, Wang Z, Felser C, Aroyo M I and Bernevig B A 2017 *Nature* **547** 298

[57] Cano J, Bradlyn B, Wang Z, Elcoro L, Vergniory M G, Felser C, Aroyo M I and Bernevig B A 2018 *Physical Review Letters* **120** 266401

[58] Nakamura T, Souma S, Wang Z, Yamauchi K, Takane D, Oinuma H, Nakayama K, Horiba K, Kumigashira H, Oguchi T, Takahashi T, Ando Y and Sato T 2019 *Physical Review B* **99** 245105

[59] Chiu Y C, Chen K W, Schönemann R, Quito V L, Sur S, Zhou Q, Graf D, Kampert E, Förster T, Yang K, McCandless G T, Chan J Y, Baumbach R E, Johannes M D and Balicas L 2019 *Physical Review B* **100** 125112

[60] Zhang S and Yazyev O V 2025 *Physical Review B* **112** 165147

[61] Zhang S, Wu Q, Liu Y and Yazyev O V 2019 *Physical Review B* **99** 035142